Part One
From Research to Application

1

Nanophotonics: From Fundamental Research to Applications

François Flory,[1] Ludovic Escoubas,[2] Judikael Le Rouzo,[2] and Gérard Berginc[3]

[1]Ecole Centrale Marseille, 38 rue Frédéric Joliot-Curie, 13013 Marseille, France
[2]IM2NP, Faculté des Sciences et Techniques, Avenue Escadrille Normandie Niemen, Service 262, 13397 Marseille Cedex, France
[3]THALES Optronique SA, 2 Avenue Gay Lussac, 78990 Elancourt, France

1.1

Introduction

Nanophotonics is a very active field of research. The understanding of fundamental phenomena and the progress in technologies have already made possible numerous applications and a large number of new applications will certainly come up in the near future. After a brief introduction, we will present some concrete examples using nanophotonics concepts to make performing optoelectronic components and how this process has been implemented. Because of wave–corpuscle duality, light's nature and its propagation can be described with a whole set of parameters. Amplitude, phase, wavelength, polarization concern the wave part, when spin, orbital momentum, or energy are used to describe the elementary quantum of light called photon. The nature of the photon is still in discussion [1]. The spin angular momentum and the orbital angular momentum of photons are linked to the polarization and the phase of the wave, respectively. The number of photons and their energy are linked to the amplitude and the wavelength of the wave. Thanks to both availability of numerical models and progresses made in nanotechnologies, the control of one or several of these parameters paves the way for numerous fields of applications. Optical properties of materials can be now mastered with subwavelength structures with remarkable performances. Components with still smaller size can be developed leading to very compact complex systems in diverse industrial fields such as telecommunications, optical interconnections, sensing, solar energy harvesting, imaging, health, security, lighting, and so on. The development and research in this field goes through the understanding of optical phenomena at a very small scale [2]. It is then necessary to develop models and to analyze the properties of the nanostructures. A remarkable progress has been achieved in the past two decades in

Micro- and Nanophotonic Technologies, First Edition. Edited by Patrick Meyrueis, Kazuaki Sakoda, and Marcel Van de Voorde.

terms of numerical tools becoming available to solve electromagnetic problems and the formulation of nanostructures with plasmonics, quantum structures, and so on. When materials are structured at the scale of the light wavelength or a fraction of the wavelength, optical waves are diffracted and scattered, and the multiple waves obtained can interfere together. The mastering of such structures can be used to control the spatial distribution of the light and its phase, its polarization, or its spectral distribution. Periodic structures diffract the incident light that is then distributed in different discrete propagation directions. It is the wide field of diffractive optics [3], which aims at making components capable of changing the shape of an optical beam. The so-called photonic crystals can be made by associating different materials with periodic structures [4]. Photonic crystals have already a large number of applications such as chemical and biological sensors, solar cells, controlled light emission, organic light emitting devices, very small-dimension integrated optical circuits, low threshold lasers, optical interconnections, and so on. Similar to electronic properties, the optical properties of PCs can be described with Bloch functions and band diagram. The optical density of states can be engineered by designing PCs. With structures of small portions of the wavelength, combinations of dielectric, semiconductor, or metallic materials are used to design metamaterials with properties not readily available in nature. The effective electric permittivity ε and magnetic permeability μ of metamaterials can be tuned, allowing the control of the propagation of electromagnetic waves. It is then possible to obtain unusual properties such as $\mu=\varepsilon=0$ or a negative value for ε and μ [5], or materials acting on the orbital angular momentum of light [6]. Today, potential applications of metamaterials concern all waves. Of course, metamaterials can be designed not only for optical waves and microwaves but also for ultrasonic wave, earthquake, and even tsunami. Superlenses [7], sensors [8], invisibility cloak [9], efficient and compact RFID antennas [10], and shielding from earthquakes or sea waves [11] are some of the applications considered. Applications using the design of the orbital angular momentum concerning optical tweezers [12], free space optical communications [13], and cryptography [14] have been already demonstrated in research laboratories. When the surface structure is random, light is diffracted in different directions of space. This light distribution can be controlled by choosing the statistic of the random surface, and this paves the way for new classes of optical components. The surface between a metal and a dielectric can support the so-called plasmon resonance. Such resonance of the electromagnetic field is also possible with metallic nanoparticles of a few tens of nanometers. The scientific field concerning this phenomenon is called plasmonics. The corresponding electric field enhancement can be used for numerous applications, such as subwavelength photonics components, and processes, such as surface-enhanced Raman scattering, light harvesting for solar cells, local heating, sensors, imaging, and so on. Metallic nanostructures can also be seen as optical nanoantennas converting freely propagating optical waves into localized field and vice versa [15]. Because of the very small scale of such structures the field is in its infancy. By similarity to radio waves and microwaves, rectifying structures can be designed at optical frequencies, but the interaction of light with the whole metallic nanostructures and the strong local field generated makes the physics different and still needs research. When one or several dimensions of semiconductor crystals are of a few nanometers, below the thermal de Broglie wavelength, electron and hole confinements occur at room temperature. Then, the electrons and holes can take only discrete values of energy in the valence band and conduction band that depend on the size. So, the electrons in a quantum dot (QD) behave like in an atom with different discrete possible energies [16]. This has, of course, direct consequences for the optical properties [17]. Quantum wells made of semiconductor layers limited in 1D are widely used for many years to make semiconductor lasers [18] or photodetectors [19]. QDs have many applications, in particular, for single-photon generation, and they are used to enhance solar cell efficiency [20], as biologic tags, and for light sources (QLED), emissive displays, QD laser, and so on.

1.2
Application of Photonic Crystals to Solar Cells

The production of renewable energy must be developed. Photovoltaic solar cells are rapidly progressing since a decade. The goal is to make both low-cost and high-efficiency solar cells, with environment-friendly materials. Different organic materials are good candidates, but they generally lead to devices that are low on efficiency. In particular, because of the small diffusion length of excitons and charges, they are made of films of thickness no larger than 100 nm. The light from the sun must be fully absorbed in this thickness on the largest spectra possible. A thin-film solar cell is made of a stack of different layers. Different absorbing materials can be used. They are often associated with (6,6)-phenyl-C_{61}-butyric-acid-methyl ester (PCBM), which is used as a hole transport material. The first approach to increase the efficiency is to optimize the structure for an optical field enhancement in the thin active layer [21]. It is also possible to use Bragg reflectors [22]. Some materials such as poly-3-hexylthiophene (P3HT) exhibit a very high absorption in the visible but a weaker absorption in the near infrared, above 600 nm. Two-dimensional photonic crystals (PCs) can be used to enhance the near-infrared light path and to trap it in the small volume of the active layer [23]. The design of PCs can be made using different numerical tools. In Ref. [23], the finite difference time domain (FDTD) method is used to calculate the band diagram of a 2D nanowire array made in the active P3HT/PCBM layer by solving Maxwell equations versus time, with a discrete spatial grid. The result of the calculation for the structure shown in Figure 1.1 is given in Figure 1.2. The vertical axis corresponds to the electromagnetic wave frequency and the horizontal axis is the propagation direction. M,Γ, X represent high-symmetry wave vector directions in the first Brillouin zone. As can be seen in the part surrounded by a semicircle, the curves representing the Bloch mode may exhibit a horizontal extremum at normal incidence Γ. It corresponds to

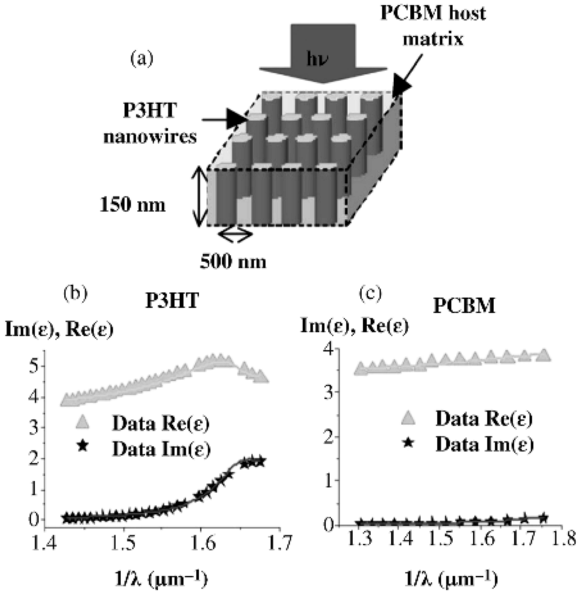

Figure 1.1 (a) P3HT/PCBM nanostructured in the form of a photonic crystal: ordered heterojunction composed of P3HT nanowires embedded in PCBM. (b) P3HT complex dielectric constants. (c) PCBM complex dielectric constants [23].

light trapped in the layer in a leaky guided mode, so that the absorption is stronger for the corresponding wavelengths (Figure 1.3). The optimization has also been performed for the structure shown in Figure 1.4 with the photonic crystal made in the blend heterojunction P3HT/PCBM [24]. The thicknesses of each layer composing a solar cell have also been optimized to obtain the largest

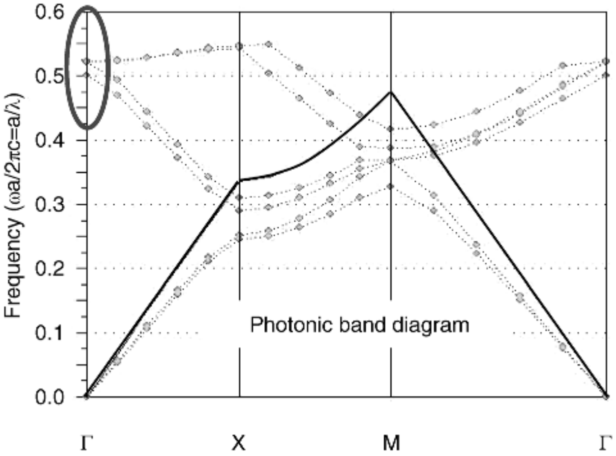

Figure 1.2 Band diagram of the structure shown in Figure 1.1a [23].

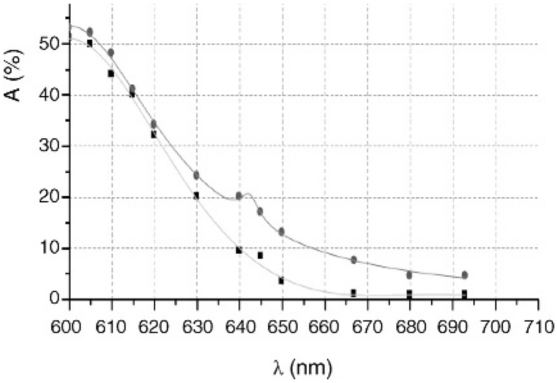

Figure 1.3 Absorbance of P3HT:PCBM blend (bulk heterostructure) (■) and of P3HT/PCBM photonic crystal of Figure 1.1a (•) [23].

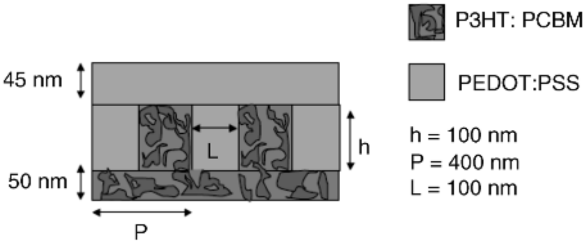

Figure 1.4 Photonic crystal made in the blend heterojunction P3HT/PCBM [24].

optical field in the active layer and so the largest efficiency. The electrical conduction must also be optimized in particular by using a smaller PEDOT:PSS layer thickness possible. The efficiency is increased from 3.7 to more than 4% with the best design. It must be noticed that the photonic crystal nanostructure can be made by nanoimprint (Figure 1.5). The interest of PCs has also been

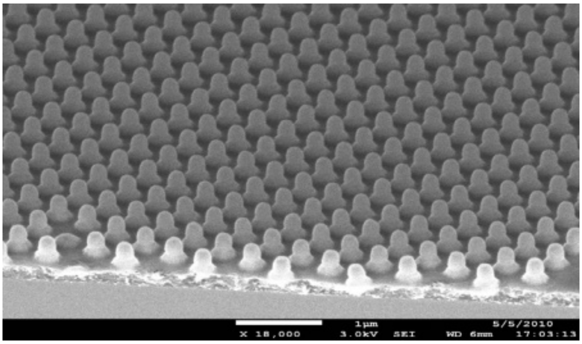

Figure 1.5 Photonic crystal made by nanoimprint in a P3HT/PCBM blend (Laboratoire des Technologies de la Microélectronique).

shown for silicon thin-film solar cells [25]. An increase in the integrated absorption in the wavelength range of interest up to 45%, instead of 33% for the not patterned, has been obtained with a 100 nm thick amorphous silicon layer.

1.3
Antireflecting Periodic Structures

Inspired by the AR properties of moth eyes [26], surface structures have been studied to reduce the reflection on large wavelength ranges. Such a nanostructure can also be found on cicada wings to make them very transparent (Figure 1.6). The structure not only helps the cicada to hide from its predators but also exhibit hydrophilic, antibacterial, and self-cleaning properties. Silicon surface has a reflection coefficient of around 30% in the near and medium infrared. Coatings can be deposited to reduce this reflection, but the effect is limited to a small spectral range. An artificial structure made of an array of nanopyramids of 1 μm biperiodicity has been studied, because it is quite easy to obtain by conventional chemical etching [27]. The basic principle underlying the effective index of lacunar materials is that when the period is small in front of the wavelength, the incident light will cross through a material of progressively changing density from air to bulk, so that the Fresnel reflection is suppressed. However, it has been shown [27] that even structures with a period close to the light wavelength can have excellent antireflecting properties. The advantage of using truncated pyramid (Figure 1.7) has been shown by FDTD simulation (Figure 1.8). The AR effect of the structure is limited to the infrared band II, between 3 and 5 μm. In nature, as observed in moth eyes, antireflective surfaces exhibit two levels of structure. One structure is made of a short-range subwavelength hexagonal periodic pattern and a "quasi-crystalline" random arrangement of the hexagonal pattern [28]. So, other artificial structures made of double-period pyramids, sand castle like, have been studied (Figure 1.9) [29]. Calculation shows that, in this case, the AR effect is extended below 3 μm, down to the visible. From an experimental point of view, excellent results are obtained with top-flat and top-patterned cone grating made by deep UV lithography and plasma etching in

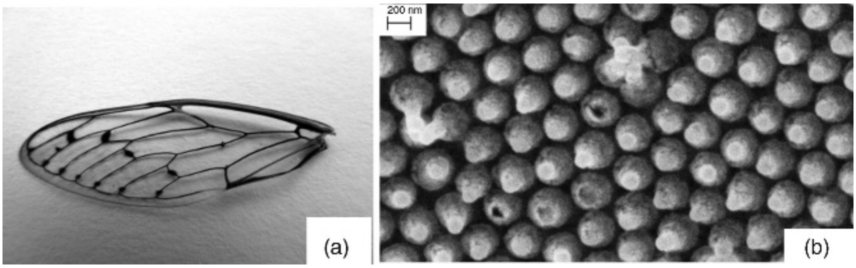

Figure 1.6 (a) Transparency of a cicada wing. (b) Nanostructure of a cicada wing (antireflecting, hydrophobic, autocleaning, and antibacterial).

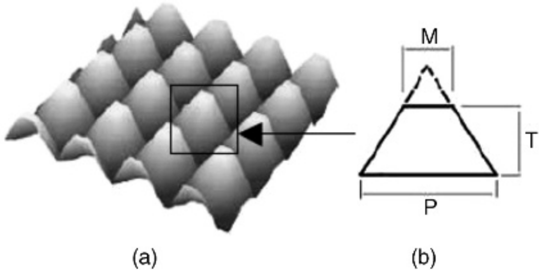

Figure 1.7 (a, b) Array of nanopyramids of $P = 1$ μm biperiodicity made in silicon by conventional chemical etching [27].

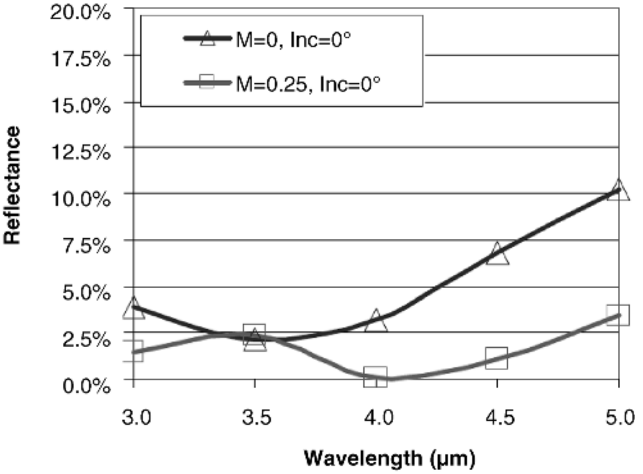

Figure 1.8 Reflectance of a width *M* of the flat part of the pyramids at normal incidence [27].

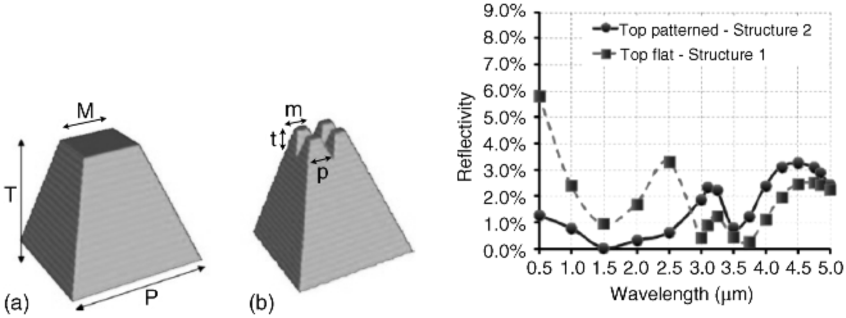

Figure 1.9 Calculated reflectivity of top-flat (a) and top-patterned (b) nanopyramid arrays. $P = 1$ μm, $M = 0.5$ μm, $T = 1.25$ μm, $m = 0.125$ μm, $p = 0.25$ μm, $t = 0.3125$ μm [29].

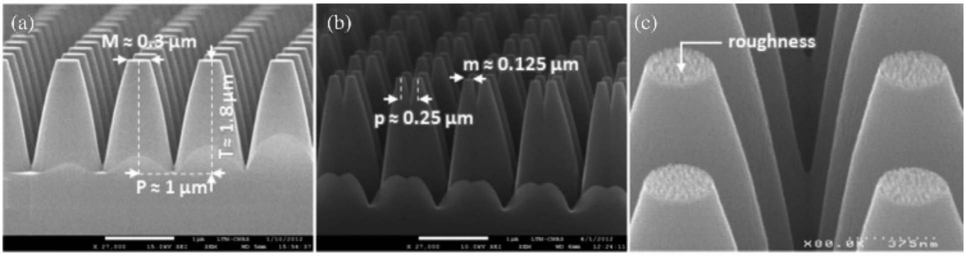

Figure 1.10 TEM pictures of truncated flat-top (a), patterned-top (b), and rough-top cone gratings (c) [30].

silicon [30] (Figure 1.10a and b). Instead of patterning the top of the cones with periodic structure, the surface can be made rough (Figure 1.10c) [30]. The reflectance spectra of flat-top, patterned-top, and rough-top cone gratings measured in the visible by integrating sphere and in the IR by FTIR spectrometry are compared in Figure 1.11.

1.4
Black Silicon

The silicon surface texturing has been studied in recent years to minimize the optical reflectance of this semiconductor material used in many optoelectronic applications, particularly in the field of photovoltaics [31] or CCD or CMOS imagers. Structured surfaces can indeed reflect much less light than the polished surfaces. If the results with periodic surfaces have certain limits, angular and spectral, as well as some side effects (creation of diffraction orders), the use of random rough surfaces allowed to improve further the quality of the antireflection (lower reflectance and better angular acceptance). This decrease of reflectance is partly related to the height of roughness. Thus, many studies now focus

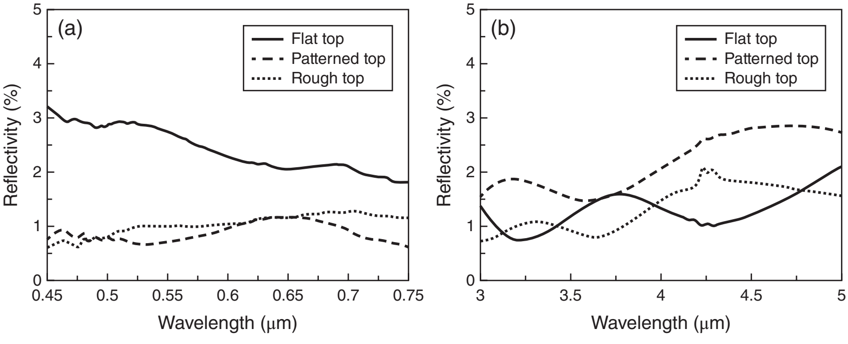

Figure 1.11 Reflectance spectra of flat-top, patterned-top, and rough-top cone gratings measured (a) in the visible by integrating sphere and (b) in the IR by FTIR spectrometry [30].

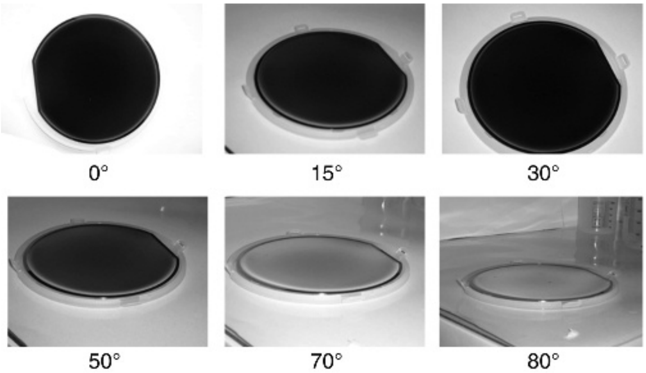

Figure 1.12 Flash photographs of black silicon at various incidences. Beyond 50° incidence, backscattering increases again.

on the highly rough materials. When the degree of roughness is sufficient, silicon visually appears dark. The result is what is known as "black silicon," whose appearance becomes perfectly black and is, therefore, extremely absorbent of visible wavelengths, even for large angles of incidence up to about 50° (Figure 1.12). The interest to fabricate black silicon is multiple. In addition to reduce the reflectance, the use of black silicon in a photodetector allows to improve its sensitivity. It is then possible to increase the photoresponse in spectral ranges of low absorption, that is, for infrared wavelengths between 900 and 1100 nm. The origin of black silicon dates back to 1980. During plasma etching processes of silicon, dark spots appeared in some areas. After electron microscopic observation, it was found that these dark areas were actually composed of a set of micrometric needles. The first work that stresses the importance of black silicon dates back to 1995 with the description of "the black silicon method" as a universal method to determine the parameters for a profile control of trenches obtained in silicon by etching in fluorine plasma [32]. In this work, the appearance of black silicon, that is, nanowire-like structures on the surface of silicon, allowed to demonstrate not only excellent setting parameters such as flow rate of SF_6 and O_2 for engraving but also partial pressure of the gas and power injected to the plasma. This excellent setting, complemented by a third CHF_3 gas type, allows for vertical walls to be obtained and controls the pattern profiles etched into the silicon, which is an essential element for the density of components made in the microelectronics industry. Beyond plasma etching techniques, other methods provide also black silicon, each leading to a type of black silicon composed of different structures. Three production methods by chemical etching, by plasma etching, and by femtosecond laser are detailed in the following paragraphs. The chemical etching of silicon can be obtained with different solutions [33,34]. The detailed chemical process here is based on a given redox reaction possible by the presence of a metal catalyst, in our case silver. The etching solution comprises an aqueous mixture containing hydrofluoric acid (HF) and silver nitrate ($AgNO_3$). Silver ions bind to the surface of the silicon, causing the creation of silver particles on the surface of silicon. This forms a layer of SiO_2 in the area below the silver particle. This layer is etched by the hydrofluoric acid solution. By oxidation and successive etchings, capillaries are etched in silicon. A 45 min etching allows the production of several micrometers high nanowires, such as those presented in Figure 1.13. The final step of removing the remaining silver particles is necessary. It is performed using a HNO_3 bath. Plasma reactive ion etching (RIE) is widely used in micronanoelectronics industry [35]. Considered as adverse effects, early studies were designed both to understand the formation mechanisms and to limit the appearance of black silicon structures. On the contrary, other techniques used to etch silicon by plasma enabled the creation of black silicon [36]. Only two techniques are presented here. These techniques are representative of the most commonly described methods in literature. Both presented plasma etching processes that enable the creation of black silicon are the Bosch process and the cryogenic process. Both are commonly used for silicon etching in the microelectronics industry [37]. The Bosch process was developed to meet the deep etching needs. It is one of the processes of deep reactive ion etching (DRIE) allowing to obtain high form factors (e.g., 20/1). The Bosch process is based on the alternation of two steps. The first step is to perform an etching using a specific gas (SF_6 for silicon). This isotropic etching is performed in a short time. Passivizing the plasma is then performed using C_4F_8 gas type allowing a polymer film of C_2F_6 or C_2F_4 or C_4F_{10} type to be deposited. A new plasma-based SF_6 step allows, then, to eliminate the passivation in the bottom of the structure and to etch the silicon in depth. By alternating the etching and passivation steps, it is possible to obtain high form factors. However, alternating passivation and isotropic etching generates etching width variations, which are all the more important in the sense that the etching phases are long. Another drawback that may appear is the deposition of the passivation polymer on the walls of the etching chamber, which can lead to variation of the species present in the chamber and, therefore, etching parameter drift. The Bosch process has, however, the advantage of being a feasible

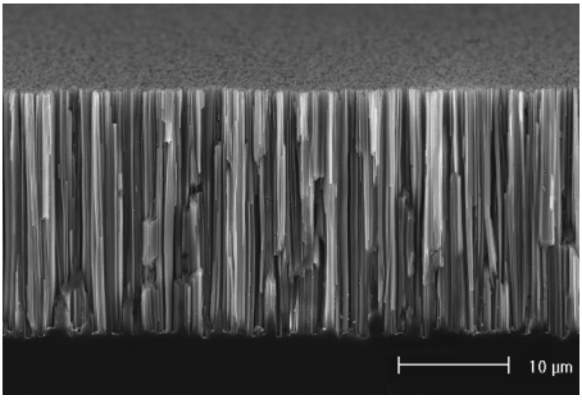

Figure 1.13 Silicon nanowires obtained by chemical etching (IM2NP).

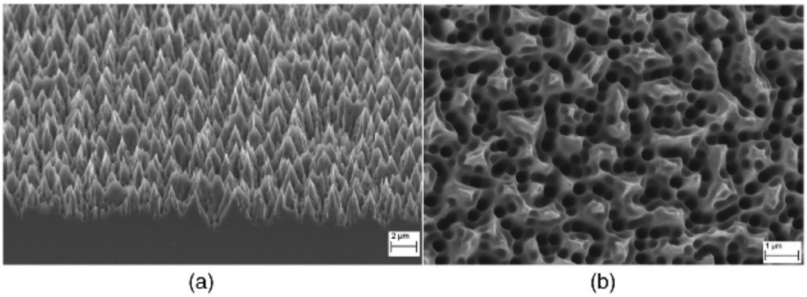

Figure 1.14 Black silicon by cryogenic plasma process. Electron microscope images: inclined view (a) and top view (b).

technique at room temperature. The use of a cryogenic process is necessary for the passivation and etching in a single step. Unlike the Bosch process, the passivation effect is obtained during the etching step. The etching plasma is again obtained using SF_6, but in this case, oxygen is added. Oxygen is used to create a SiO_xF_y layer on the flanks of the structure. To create this passivation, silicon must be cooled down to low temperatures, hence the name of cryogenic process [38]. Compared to the Bosch process, the etching rate can be up to twice as high (Figure 1.14) while allowing to obtain smooth profiles. The major drawback of this technique is that the silicon surface temperature must be precisely controlled. For this technique, the silicon has to be brought to a temperature typically approaching −100 °C. Other plasma etching methods also allow the production of black silicon. One can, for example, note the work of Inomata *et al.* [39], which presents a RIE process under a Cl_2 atmosphere. More recently, the Eric Mazur's research team at Harvard was the first to study the fabrication of very rough surfaces of silicon (Figure 1.15) by successive femtosecond laser pulses in gas (SF6) [40–44]. Furthermore, this black silicon is doped at the surface by the atoms present in the gas, especially sulfur. This surface doping significantly widens the silicon absorption spectrum in the near infrared, beyond the 1.1 μm wavelength. Indeed, by its manufacturing process, the Mazur group's black silicon contains trapped sulfur atoms at the silicon surface. If we consider

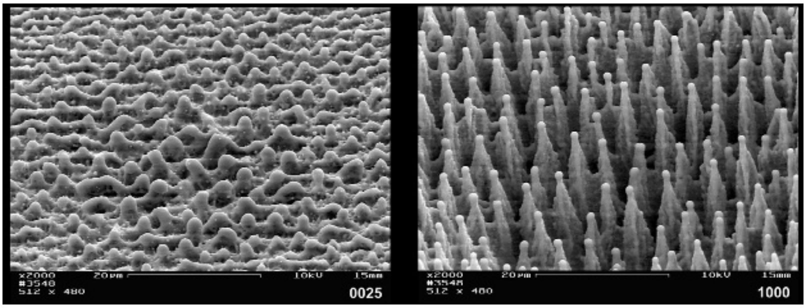

Figure 1.15 Black silicon fabricated by femtosecond laser structuring (Mazur's team).

an energy diagram of silicon, the valence band and the conduction band are separated by a 1.12 eV energy gap. By the addition of another element in a high concentration, an intermediate band can be created. This intermediate band must be made of a material enabling absorption at energies lower than the band gap. In low concentrations, the dopant shows discrete energy levels. When the concentration increases and reaches concentration values close to the per cent, the discrete levels become energy bands. This is the explanation proposed by Mazur for sulfur integration into silicon. Energy levels at 0.371 eV, 0.318 eV, and 0.188 eV would form an intermediate energy band allowing photons of energies lower than 1.12 eV to be absorbed. In the case of materials created by the Mazur's team, the infrared absorption of silicon offers the possibility to fabricate photodetectors working at near-infrared wavelengths, that is, in a wavelength range, which is covered by cooled detectors (InGaAs type). The Mazur's team has licensed its technology to SiOnyx, a startup, which sells imaging sensors comprising black silicon for night surveillance applications. For applications related to photovoltaics or imagers, black silicon has major advantages such as the increase in photocurrent by a better photon harvesting for the solar cells [31,45–47] or the improvement of sensitivity and the extension to infrared wavelengths for the imagers [33,34]. Since 2010, the IM2NP and Thales Optronique [48] explored the possibility of fabricating black silicon by a novel method of random dry etching the silicon surface without photolithographic mask. This work resulted in a patent application [49]. Since then, several research teams around the world have evinced interested in black silicon in terms of fabrication by etching [50–52] and modeling [53,54].

1.5
Metamaterials for Wide-Band Filtering

Complex optical wave filter functions can be made with metamaterials. We consider here the example of a study on a filter having a reflectivity smaller than 15% in the visible near IR and short wavelength IR, up to 2.5 μm, and a reflectivity more than 90% in the mid-IR region and far IR, between 3 and 5 μm (Figure 1.16). There are different applications of this kind of filter such as stealth vehicles or in thermophotovoltaics for which the wavelength up to 2.5 μm must be converted in electrons while limiting the emissivity for longer wavelengths. Different structures have been studied [55,56]. The best result is obtained with the structure shown in Figure 1.16. It is made of inverted cone grating coated with a tungsten film on a flexible substrate. The period is 1 μm, the inverted cone depth is 1.8 μm, and the tungsten thickness is of 200 nm. The structure has been made by imprinting a truncated cone grating made on a silicon surface in a PVDF polymer substrate. The tungsten layer is then deposited by magnetron sputtering (Figures 1.17 and 1.18). The measured transmission of this filter is given in Figure 1.19. A simulation made by the field mode-matching method has been performed for perforated tungsten substrate with the same period.

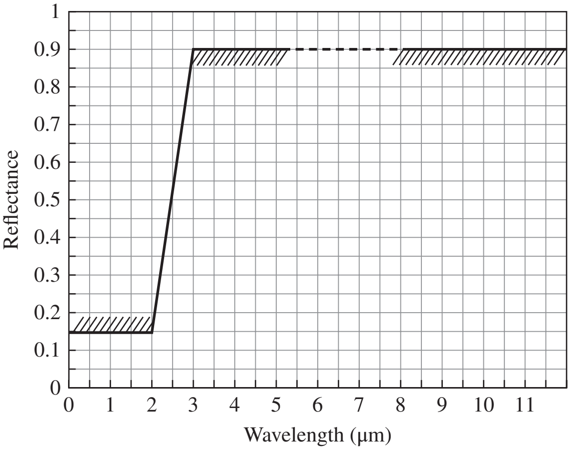

Figure 1.16 Targeted reflectance [56].

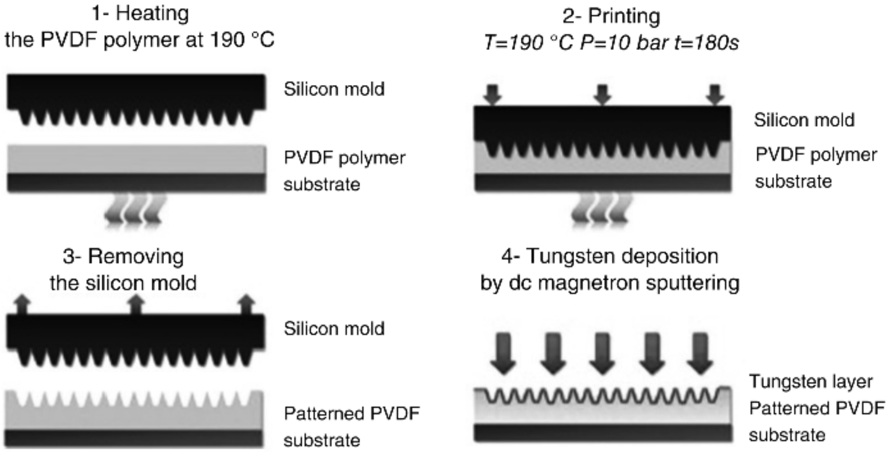

Figure 1.17 Realization technique [56].

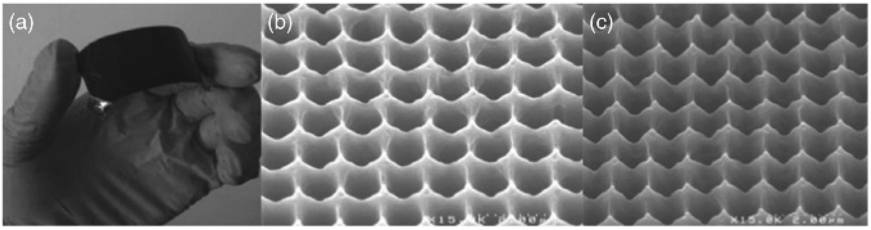

Figure 1.18 (a) Metamaterial filter deposited on a flexible substrate, (b) inverted cones before depositing tungsten, and (c) after depositing tungsten [56].

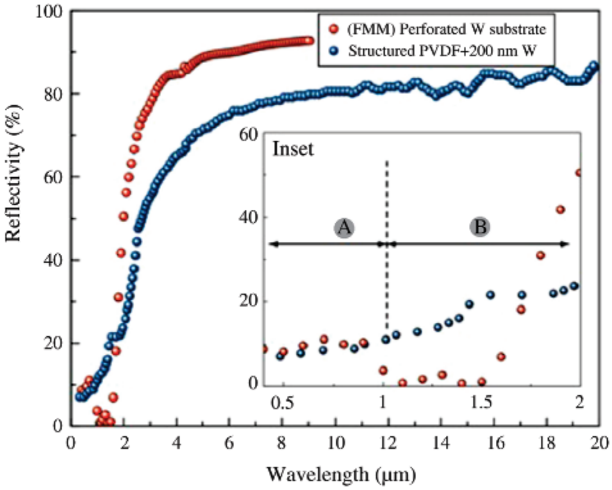

Figure 1.19 Calculated reflectivity of a perforated tungsten substrate and measured reflectivity of the inverted cone-structured PVDF coated with 200 nm of tungsten. The inset is a zoom in the 4–2 μm wavelength range [56].

1.6
Rough Surfaces with Controlled Statistics

In optical systems, surface roughness induces light scattering that generally reduce their performances. However, when controlling the surface roughness, statistic optical functions can be obtained [57,58]. As seen in the next paragraph, a rough surface can improve silicon detector performances. Random rough optical surfaces have also been used to enhance the depth of focus of imagery systems [59]. When the statistic properties of a random structure are controlled, the spatial distribution of the scattered light can be modified, for example, to have light uniformity [60] or a defined spatial shape [61]. Rough surfaces are generally composed of a large number of spatial frequencies. They can thus be decomposed as a sum of periodic patterns [62]. The amplitude distribution of the spatial frequencies corresponds to the autocorrelation function. The other main parameter necessary to qualify the roughness is the depth distribution. When making a rough surface by insolating a photoresist layer, these two parameters depend on the statistic of the laser beam speckle used and on the number of summed speckle patterns by multiple expositions. Goodman and Dainty have shown that the probability density of intensity distribution $P(I)$ of a speckle pattern in far field follows a decreasing exponential law:

$$P(I) = e^{(I/<I>)}, \tag{1.1}$$

where $<I>$ is the mean intensity and I the intensity of the scattered field. When N speckle patterns are summed, the probability density of intensity follows a

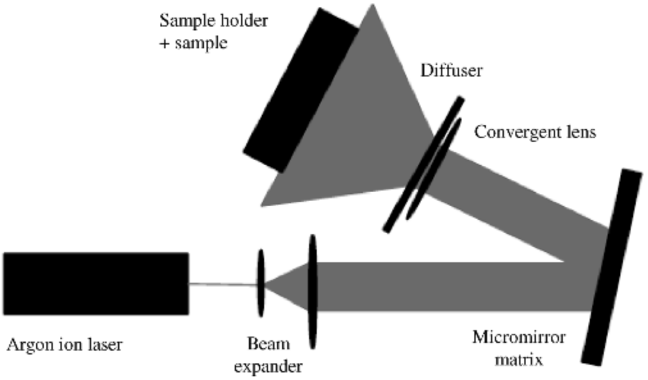

Figure 1.20 Setup used to illuminate a sample with speckle with a controlled statistic distribution [64].

gamma law of order N:

$$P(I) = \frac{I^{N-1} N^N}{(N-1)!} e^{-NI}. \tag{1.2}$$

When putting a diffusing element in front of a convergent lens used in front of the photoresist sample (Figure 1.20), Goldfischer [63] has shown that the correlation function of the speckle statistic on the sample can be linked to the square of the Fourier transform of the square of the intensity on the diffusing element. In the setup shown in Figure 1.20, the intensity on the diffusing element can be changed thanks to a computer-controlled micromirror matrix [64]. For example, the incident light can be composed of two separated beams (Figure 1.21a). The calculated 2D correlation function for the surface roughness of a photoresist insolated with this kind of illumination is given in Figure 1.21b. After being

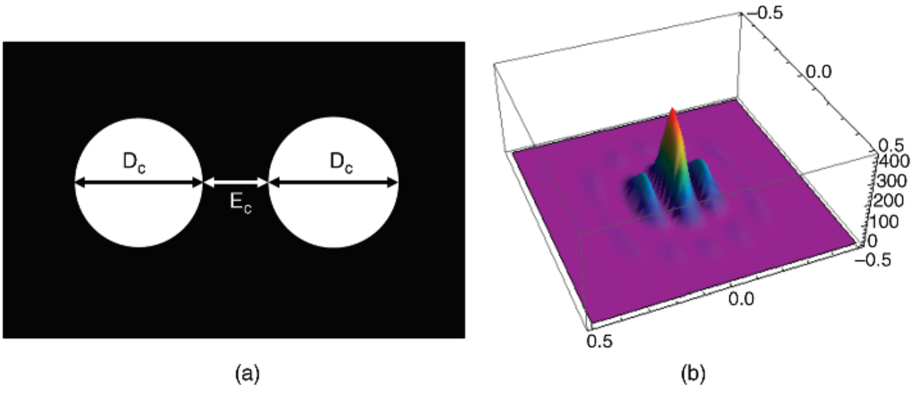

Figure 1.21 (a) Two circles aperture and (b) the corresponding correlation function [64].

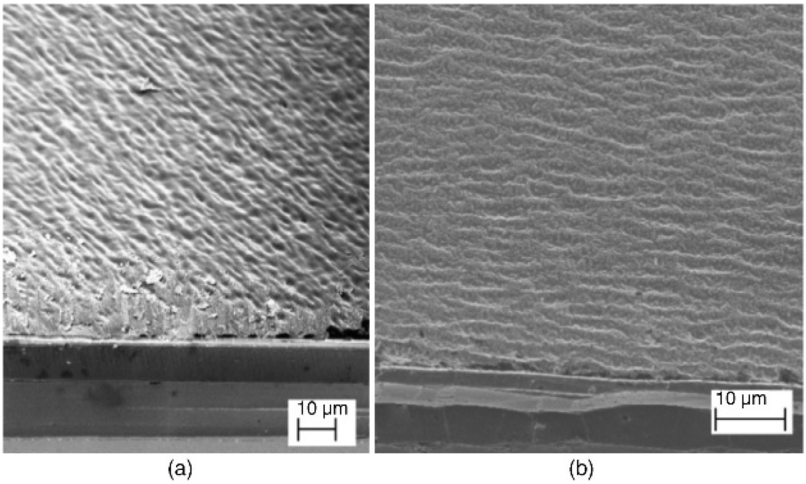

Figure 1.22 (a) Photoresist surface and (b) the silicon surface after etching [64].

exposed seven times and revealed, the photoresist deposited on a silicon wafer can be etched to transfer its structure to the silicon. Figure 1.22 shows the pictures of the photoresist surface (a) and the silicon surface after etching (b). The roughnesses of the surfaces are measured by chromatic confocal microscopy. The height distributions of the photoresist (Figure 1.23a) and of the silicon (Figure 1.23b) are in good agreement with a seven-order gamma function. With such two-beam insolation the correlation functions for the two surfaces are also in very good agreement with the theoretical one (Figure 1.24). This example shows the feasibility of making rough surfaces with defined statistics able to control the scattered light distribution.

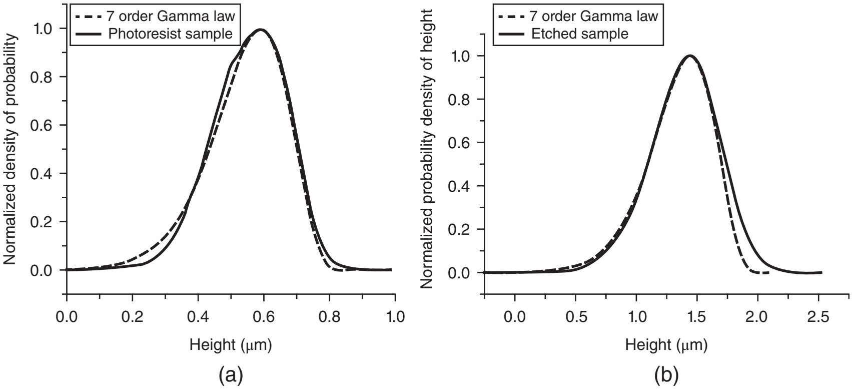

Figure 1.23 Height distribution of the roughness (full line) on (a) a photoresist surface and (b) on a silicon surface. Seven-order gamma laws are drawn in dotted line [64].

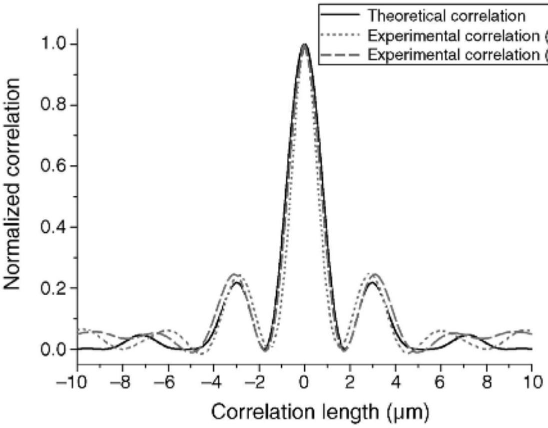

Figure 1.24 Correlation function for the roughness of the photoresist surface and of the silicon surface [64].

1.7
Enhancement of Absorption in Organic Solar Cells with Plasmonic Nano Particles

A surface separating a metallic material and a dielectric can support optical wave propagation (Kretschmann, Raether and Otto in the 1960s) [65–67]. Such electromagnetic wave is called surface plasmon. With metallic nanoparticles (NPs), plasmon resonance depends on the particle size and is redshifted in front of the surface plasmon. When considering a periodic arrangement of NPs, coupling may occur and the electromagnetic field can be strongly enhanced between the

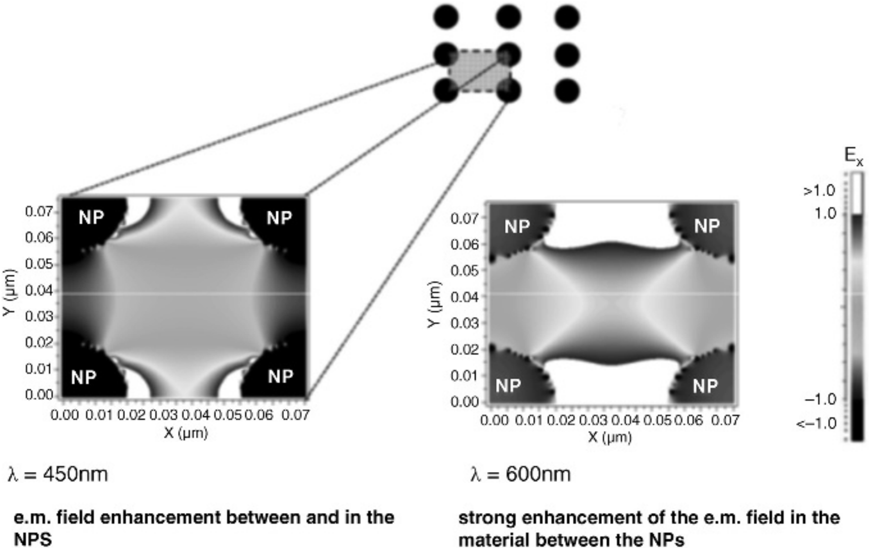

Figure 1.25 Field enhancement between metallic nanoparticles for two wavelengths.

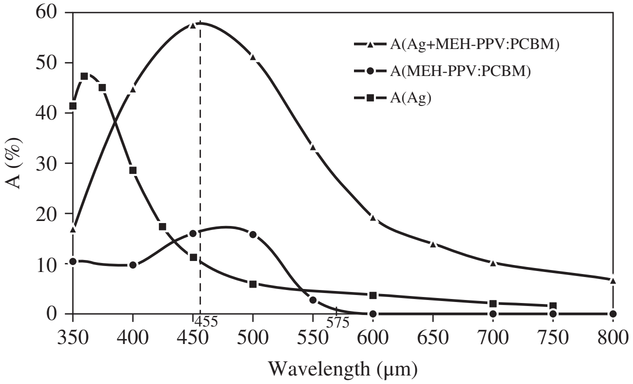

Figure 1.26 Calculated values of absorptance A = (1-R-T) versus wavelength for the devices: silver NPs in air (■), MEH-PPV:PCBM alone (•), and silver NPs embedded in MEH-PPV-PCBM (▲). MEH-PPV is poly(2-methoxy-5-(2-ethyl-hexyloxy)-1,4-phenylenevinylene and PCBM is a fullerene derivative (6,6)-phenyl-C_{61}-butyric-acid-methyl ester [70].

NPs, breaking the diffraction limit for the localization of light into subwavelength dimensions. FDTD calculation results for 70 nm biperiodic grating made with 40 nm diameter NPS in an organic layer for PV are shown on Figure 1.25. The fields are shown for a wavelength of 450 nm and for the resonant wavelength of 600 nm. The use of metallic nanoparticle is well known to tremendously enhance the Raman spectroscopy signal [68]. The single-molecule enhancement factor (SMEF) that quantifies the increase in signal intensity per molecule varies from 10^4 to 10^{12}. Metallic NPs have also been studied to increase the light absorption in organic solar cells since 2000 [69]. Different positions of silver NPs' structure have been investigated. A detailed study on the particle size, grating period, and positioning in the active organic layer has been led by Savin *et al.* [70]. Both calculation and experiment show that a strong increase in the absorption can be obtained in a wavelength range for which the active material alone is only weakly absorbing (Figure 1.26).

1.8
Quantum Dot Solar Cells

In semiconductor nanocrystals of a few nanometers, the electron states are discrete and the band gap can be tuned not only by changing the semiconductor material but also by changing the size. When the nanocrystal is a sphere, one speaks about quantum dots (QDs). The use of colloidal QDs [71] to make solar cells with low-cost process shows a great potential. These concentrated nanoparticle solutions are stabilized by long hydrocarbon ligands that keep the nanocrystals suspended in solution. With core–shell structures, the photogenerated charges are trapped in the QDs leading to high-efficiency luminescent materials. They can be used in front of solar cells to give down conversion frequency changing UV wavelengths into more efficient visible light [72]. However, charge transfer is then limited to the use of such core/shell structures for charge generation. Colloidal QDs without shell have a surface covered with organic ligands. The ligand can be suppressed or their length can be engineered to optimize charge transfer to an organic matrix. Electronic and optical properties of the hybrid QDs/organic materials must be modeled both to optimize both charge generation and band alignment and to maximize the optical field in the generally thin hybrid active layer [73]. The electronic properties of QDs can be calculated with rigorous *ab initio* theory like the semiempirical pseudopotential method [74] and the function density theories [75]. As these calculations are complex and computer time-consuming. they are not well adapted to design structures. Approximate calculation techniques such as multiband *kp* [76] can give excellent approximation but are still too computer time-consuming and needs numerous parameters. Effective mass approximation (EMA) allows simple and very fast calculation techniques with few parameters. In a solid, charge behavior depends on the local fields. To take into account this dependence, it has been proposed to replace the mass of a charge by another mass that leads to an equivalent behavior of the charge. Then, the material can be considered as homogeneous. In very thin semiconductor films, called quantum wells, the resolution of static Schrödinger equation gives the wave function of the electrons or holes and their possible discrete energies. The solutions can be found by different techniques such as the transfer matrix method (TMM) [77] or by the ballistic method [78]. The EMA have its own limits, but it can be extended to take into account the nonparabolicity of the electronic properties by using a modified mass formulation [79]. This approach allows to explain very accurately the measured band gap of most semiconductor nanocrystals of different sizes. An example of such a calculated result and the measurement of conduction and valence band edges measured by cyclic voltammetry [80] are given in Figure 1.27. It is also well adapted for multiquantum well calculation. The method can be extended to nanowires and core/shell quantum spheres. The optical properties of quantum structures depend on the electronic properties. Each possible transition between two electronic levels gives a resonant frequency of absorbance. The value of these frequencies depends on the energy levels concerned, taking into account the shift induced by the binding energy of the excitons. It can be interband transitions, between the conduction and the valence bands or intraband transitions. A single frequency resonant system can be modeled with a harmonic oscillator. The absorption level depends both on the density of states, which can be evaluated from thermodynamic considerations, and on the associated oscillator strength. Thermal and size dispersion effects enlarge each absorption band. The electronic states can also be coupled. In QDs, surface traps or recombination centers can be important. Impurities and structure defects must also be considered. So, it appears to be quite difficult to fully model the spectral absorption of quantum structures and so is the dielectric function. However, the complex refractive index can be determined from the measured absorption spectrum. Solar cell efficiency depends on the absorbed spectrum

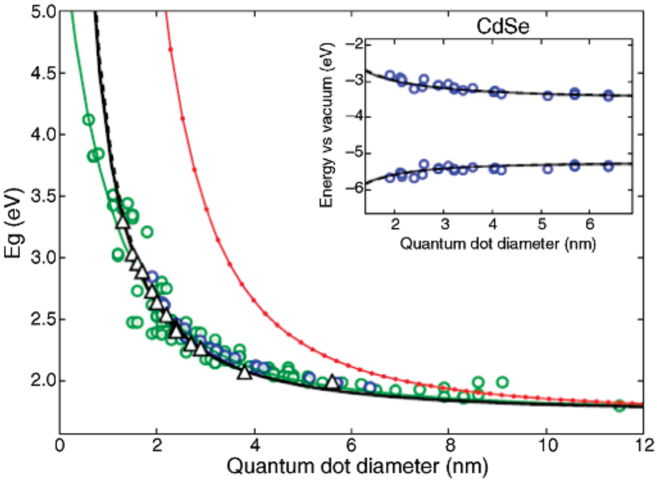

Figure 1.27 Calculation of the band gap of CdSe nanospheres with (solid line) and without (dashed line) the nonparabolicity correction. Comparison between semiempirical pseudopotential calculation (triangles) and experimental data (circles) from the literature [79]. The results with Brus equation are also shown (dotted line). The inset shows the results in comparison to conduction and valence band edges measured by cyclic voltammetry [80].

that is directly related to the band diagram of the semiconductor used and, with QDs, on their size. As already explained, the control of this band diagram, and thus that of the quantum dot, allows us to get a large absorption spectral scale by mixing different materials. Depending on the colloidal QD absorption coefficients value (either high or low in the solar spectral range), light management is one issue to provide a path for enhanced current collection in QD solar cells. Indeed, in these kinds of devices, a compromise between absorption and extraction must be found. In this way, different photonic approaches can be considered in order to enhance the absorption in quantum dot solar cells, such as nanophotonics for designing light-trapping schemes [81] or surface plasmon resonances by using metallic nanoparticles [82]. Newly mastered fabrication methods make possible the realization of these photonic structures, which could be realized either on single junction or on other solar cell concept. Among the latter, the QDs can be integrated for using in the multijunction, either in multiexciton generation (MEG) or in hot carrier solar cells. The aim of these two is to overcome one of the limiting mechanisms of a single-junction solar cell, by using the energy excess of the generated exciton. For instance, the MEG concept occurring in a quantum dot allows the generation of several charges from one UV photon [81]. The best results are obtained with low band gap QDs such as PbS, PbSe, or InP. Different sizes and materials can be associated with harvesting different parts of the solar spectrum in multijunction structures. Coupled QDs change discrete energy levels into energy bands. Associations of several layers of QDs of different sizes are studied to make multi junction solar cells [82].

Theoretically, such solar cells may have up to 48% efficiency for three active layers. A first proof of concept of a tandem structure (Figure 1.28) shows the possibility of using two different band gaps (PbS quantum dots with two different sizes) in such architecture. Although the open-circuit voltage is good enough, the critical issue is the optimization of the recombination layer for the matching and the collection of the photocurrent. In this frame of multijunction solar cells, we can also imagine the use of just one QD layer in order to get the requisite band gap for optimizing the complete stack of the cell, absorbing in a large spectral part. Another concept using QDS is the hybrid quantum dot solar cells. Hybrid solar cells, whose active layer is a blend of a polymer material and inorganic nanoparticles, have benefited in recent times from substantial work, allowing better assessment of the mechanisms occurring at the interface organic/inorganic nanoparticle. Indeed, different effects can limit the performances of hybrid QDSCs [62]. The QDs may have surface traps and they have to be passivated; QDs coupling changes discrete energy levels in energy bands; the electrons and holes must be efficiently transferred to the electrodes and they are separated by associating n-type and p-type semiconductors with percolated paths; band alignment is also mandatory to be considered by choosing materials with appropriate electronic affinity [83]. However, very rapid progresses are being made, giving great expectations for this kind of solar cells. These studies can also be transferred to different materials, such as the CIS or CZTS (Se), which have the advantage of being "without Pb and Cd free," and whose energy gap is particularly well suited to the solar spectrum.

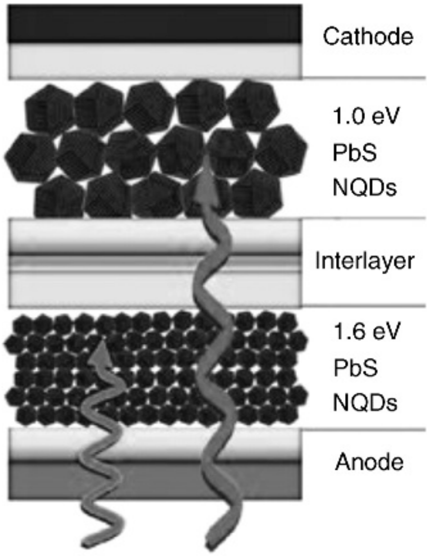

Figure 1.28 Tandem solar cell made of two different PbS QD layers, proposing optimized band gap [82].

1.9
Conclusions

From displays to imagery for biology, from fluorescent enhanced observation techniques to light trapping for solar cells, and from optical stealth to optical filters, nanophotonics is already a key technology for a very large variety of applications. We have seen through a few examples how the collaboration between a public research laboratory and a private company concerned with basic research for high-technology applications can lead to important progresses. A lot of research has still to be done in this field with very exciting emerging fundamental areas that the continuous progresses in nanotechnologies allow. For example, the mastering of the assembly of nanoparticles in more complex nano-objects will pave the way for the control of most of the properties of matter. If the support of research is as high as the stakes, this will lead to huge advances in health, telecommunications, clean energies, environment safety, and so on.

Acknowledgments

The works described in Sections 1.3 and 1.5 have been supported by the French national agency (ANR) and were conducted in collaboration with the laboratory Technologies de la Microélectronique in Grenoble, in association with companies Thales Optronique and Dassault Aviation and with the Centre d’Etude Atomique. The work discussed in Section 1.6 was undertaken in collaboration with Thalès Optronique and supported by the Délégation Générale à l’Armement (DGA) through the GENESUPRA project.

References

1 Andrews, David L. (2014) Photon-based and classical descriptions in nanophotonics: a review. *J. Nanophoton.*, **8** (1), 081599.

2 Flory, F., Escoubas, L., Le Rouzo, J., Berginc, G., and Lee, C.C. (2015) Low-dimensional optics. *J. Nanophoton.*, **9** (1), 093594.

3 Kress, B.C. and Meyrueis, P. (eds) (2000) *Digital Diffractive Optics: An Introduction to Planar Diffractive Optics and Related Technology*, Wiley-VCH Verlag GmbH, Wienheim, Germany.

4 Sakoda, K. (ed.) (2005) *Optical Properties of Photonic Crystals*, vol. 80, 2nd edn, Springer Series in Optical Sciences (eds W.T. Rhodes, T., Asakura, and K.-H. Brenner), Springer Verlag, Berlin.

5 Veselago, V.G. (1968) The electrodynamics of substances with simultaneously negative values of permittivity and permeability. *Sov. Phys. Uspekhi*, **10** (4), 509–514.

6 Gorodetski, Y., Drezet, A., Genet, C., and Ebbesen, T.W. (2013) Generating far-field orbital angular momenta from near-field optical chirality. *Phys. Rev. Lett.*, **110**, 203906.

7 Xiang, Z. and Zhaowei, L. (2008) Superlenses to overcome the diffraction limit. *Nat. Mater.*, **7**, 435–441.

8 Tao, C., Suyan, L., and Hui, S. (2012) Metamaterials application in sensing. *Sensors*, **12**, 2742–2765.

9 Alitalo, P. and Tretyakov, S. (2009) Electromagnetic cloaking with metamaterials. *Mater. Today*, **12** (3), 22–29.

10 Braaten, B.D., Scheeler, R.P., Reich, M., Nelson, R.M., Bauer-Reich, C., Glower, J., and Owen, G.J. (2010) Compact metamaterial-based UHF RFID antennas:

deformed omega and split-ring resonator structures. *ACES J.*, **25** (6), 530–542.

11 Farhat, M., Enoch, S., Guenneau, S., and Movchan, A.B. (2008) Broadband cylindrical acoustic cloak for linear surface waves in a fluid. *Phys. Rev. Lett.*, **101** (13), 134501.

12 Friese, M.E.J., Enger, J., Rubinsztein-Dunlop, H., and Heckenberg, N.R. (1996) Optical angular-momentum transfer to trapped absorbing particles. *Phys. Rev. A*, **54** (2), 1593–1596.

13 Gibson, G., Courtial, J., Padgett, M.J., Vasnetsov, M., Pas'Ko, V., Barnett, S.M., and Franke-Arnold, S. (2004) Free-space information transfer using light beams carrying orbital angular momentum. *Opt. Express*, **12** (22), 5448–5456.

14 Boyd, R.W., Jha, A., Malik, M., O'Sullivan, C., Rodenburg, B., and Gauthier, D.J. (2011) Quantum key distribution in a high-dimensional state space: exploiting the transverse degree of freedom of the photon. Proc. of SPIE. Advances in Photonics of Quantum Computing, Memory, and Communication IV, 7948, 79480L 1–6, San Francisco, California. doi: 10.1117/12.873491

15 Bharadwaj, P., Deutsch, B., and Novotny, L. (2009) Optical antennas. *Adv. Opt. Photonics*, **1**, 438–483.

16 Ekimov, A.I., Efros, A.L., and Onushchenko, A.A. (1985) Quantum size effect in semiconductor microcrystals. *Solid State Commun.*, **56**, 921–924.

17 Flory, F., Chen, Y.-J., Lee, C.-C., Escoubas, L., Simon, J.-J., Torchio, P., Le Rouzo, J., Vedraine, S., Derbal-Habak, H., Shupyk, I., Didane, Y., and Ackermann, J. (2011) Optical properties of dielectric thin films including quantum dots. *Appl. Opt.*, **50** (9), 129–134.

18 Faist, J., Capasso, F., Sivco, D.L., Sirtori, C., Hutchinson, A.L., and Cho, A.Y. (1993) Quantum cascade laser. *Science*, **264** (5158), 553–556.

19 Levine, B.F. (1993) Quantum well infrared photodetectors. *J. Appl. Phys.*, **74**, R1–R81.

20 Prabhakaran, P., Kim, W.J., Lee, K.S., and Prasad, P.N. (2012) Quantum dots (QDs) for photonic applications. *Opt. Mat. Exp.*, **2** (5), 578–593.

21 Monestier, F., Simon, J.J., Torchio, P., Escoubas, L., Ratier, B., Hojeij, W., Lucas, B., Moliton, A., Cathelinaud, M., and Defranoux, C. (2008) Optical modeling of organic solar cells based on CuPc and C_{60}. *Appl. Optics.*, **47**, C251–C256.

22 Heine, C. and Morf, R.H. (1995) Submicrometer grating for solar energy applications. *Appl. Opt.*, **34**, 2476–2482.

23 Duché, D., Escoubas, L., Simon, J.J., Torchio, P., Vervisch, W., and Flory, F. (2008) Slow Bloch modes for enhancing the absorption of light in thin films for photovoltaic cells. *Appl. Phys. Lett.*, **92** (19), 193–310.

24 Duché, D., Drouard, E., Simon, J.J., Escoubas, L., Torchio, Ph., Le Rouzo, J., and Vedraine, S. (2011) Light harvesting in organic solar cells. *Sol. Energy Mater. Solar Cells*, **95**, 18–25.

25 Park, Y., Drouard, E., El Daif, O., Letartre, X., Viktorovitch, P., Fave, A., Kaminski, A., Lemiti, M., and Seassal, C. (2009) Absorption enhancement using photonic crystals for silicon thin film solar cells. *Opt. Expr.*, **17** (16), 14312–14321.

26 Clapham, P.H. and Hutley, M.C. (1973) Reduction of lens reflexion by the "Moth Eye" Principle. *Nature*, **244**, 281–282.

27 Bouffaron, R., Escoubas, L., Simon, J.J., Torchio, P., Flory, F., Berginc, G., and Masclet, Ph. (2008) Enhanced antireflecting properties of microstructured top-flat pyramids. *Opt. Express*, **16** (23), 19304–19309.

28 Stavenga, D.G., Foletti, S., Palasantzas, G., and Arikawa, K. (2006) Light on the moth eye corneal nipple array of butterflies. *Proc. R. Soc. London*, **273**, 661–667.

29 Escoubas, L., Bouffaron, R., Brissonneau, V., Simon, J.J., Berginc, G., Flory, F., and Torchio, P. (2010) Sand-castle bi-periodic pattern for spectral and angular broadening of antireflective properties. *Opt. Lett.*, **35** (9), 1455–1457.

30 Le Rouzo, J., Brückner, J.B., Ferchichi, A., Gourgon, C., Berginc, G., and Escoubas, L. (2015) Optical properties of antireflective flat or rough patterned topped silicon cones gratings. *Adv. Device Mater.*, **1**, 23–26.

31 Liu, X., Coxon, P.R., Peters, M., Hoex, B., Cole, J.M., and Fray, D.J. (2014) Black

silicon: fabrication methods, properties and solar energy applications. *Energy Environ. Sci.*, **2014** (7), 3223–3263.

32 Jansen, H., De Boer, M., Legtenberg, R., and Elwenspoek, M. (1995) The black silicon method: a universal method for determining the parameter setting of a fluorine-based reactive ion etcher in deep silicon trench etching with profile control. *J. Micromech. Microeng.*, **5**, 115–120.

33 Koynov, S., Brandt, M.S., and Stutzmann, M. (2006) Black nonreflecting silicon surfaces for solar cells. *Appl. Phys. Lett.*, **88** (20), 203107.

34 Li, X. and Bohn, P.W. (2000) Metal-assisted chemical etching in HF/H2O2 produces porous silicon. *Appl. Phys. Lett.*, **77** (16), 2572–2574.

35 Wu, B., Kumar, A., and Pamarthy, S. (2010) High aspect ratio silicon etch: a review. *J. Appl. Phys.*, **108** (5), 051101.

36 Jansen, H., Boer, M., Legtenberg, R., and Elwenspoek, M. (1995) The black silicon method: a universal method for determining the parameter setting of a fluorine-based reactive ion etcher in deep silicon trench etching with profile control. *J. Micromech. Microeng.*, **5**, 115–120.

37 Walker, M.J. (2001) Comparison of Bosch and cryogenic processes for patterning high aspect-ratio features in silicon. *Proc. SPIE*, **4407** (0), 89–99.

38 Jansen, H., Boer, M., Wensink, H., Kloeck, B., and Elwenspoek, M. (2001) The black silicon method: a study of the performance of etching silicon using SF6/O2 -based chemistry with cryogenical wafer cooling and a high density ICP source. *Microelectr. J.*, **32**, 769–777.

39 Inomata, Y., Fukui, K., and Shirasawa, K. (1997) Surface texturing of large area multicrystalline silicon solar cells using reactive ion etching method. *Sol. Energy Mater. Solar Cells*, **48** (1–4), 237–242.

40 Myers, R., Farrell, A.R., Karger, A.M., Carey, J.E., and Mazur, E. (2006) Enhancing near-infrared avalanche photodiode performance by femtosecond laser microstructuring. *Appl. Opt.*, **45**, 8825–8831.

41 Huang, Z., Carey, J.E., Liu, M., Guo, X., Mazur, E., and Campbell, J.C. (2006) Microstructured silicon photodetector. *Appl. Phys. Lett.*, **89**, 033506–033508.

42 Winkler, M.T. (2011) Insulator-to-metal transition in sulfur-doped silicon. *Phys. Rev. Lett.*, **106**, 178701.

43 Franta, B., Pastor, D., Gandhi, H.H., Rekemeyer, P.H., Gradecak, S., Aziz, M.J., and Mazur, E. (2015) Simultaneous high crystallinity and optical absorptance in hyperdoped black silicon using nanosecond laser annealing. *J. Appl. Phys.*, **118**, 225303.

44 Yang, J., Luo, F., Kao, T.S., Li, X., Ho, G.W., Teng, J., Luo, X., and Hong, M. (2014) Design and fabrication of broadband ultralow reflectivity black Si surfaces by laser micro/nanoprocessing. *Light Sci. Appl.*, **3**, e18.

45 Jeong, S., McGee, M.D., and Cui, Y. (2013) All-back-contact ultra-thin silicon nanocone solar cells with 13.7% power conversion efficiency. *Nat. Comm.*, **4**, 2950.

46 Savin, H., Repo, P., von Gastrow, G., Ortega, P., Calle, E., Garín, M., and Alcubilla, R. (2015) Black silicon solar cells with interdigitated back-contacts achieve 22.1% efficiency. *Nat. Nanotechol.*, **10**, 624–628.

47 Otto, M., Algasinger, M., Branz, H., Gesemann, B., Gimpel, T., Füchsel, K., Käsebier, T., Kontermann, S., Koynov, S., Li, X., Naumann, V., Oh, J., Sprafke, A.N., Ziegler, J., Zilk, M., and Wehrspohn, R.B. (2015) Black silicon photovoltaics. *Adv. Optical Mat.*, **3**, 147–164.

48 Brissonneau, V. (2012) Contrôle de la lumière par des structures surfaciques désordonnées. PhD dissertation, Aix-Marseille University.

49 Escoubas, L., Brissonneau, V., Berginc, G., and Simon, J.-J. (2014) Procédé de texturation aléatoire d'un substrat semiconducteur. French patent no. 100865 FR.

50 Wang, Y., Yang, L., Liu, Y., Mei, Z., Chen, W., Li, J., Liang, H., Kuznetsov, A., and Xiaolong, D. (2015) Maskless inverted pyramid texturization of silicon. *Sci. Rep.*, **5**, 10843.

51 Nguyen, K.N., Abi-Saab, D., Basset, P., Richalot, E., Malak, M., Pavy, N., Flourens, F., Marty, F., Angelescu, D., Leprince-Wang, Y., and Bourouina, T. (2012) Study of black silicon obtained by cryogenic

plasma etching: approach to achieve the hot spot of a thermoelectric energy harvester. *Microsyst. Technol.*, **18**, 1807–1814.

52 Nguyen, K.N.D., Basset, P., Marty, F., Leprince-Wang, Y., and Bourouina, T. (2013) On the optical and morphological properties of microstructured Black silicon obtained by cryogenic-enhanced plasma reactive ion etching. *J. Appl. Phys.*, **113**, 194903.

53 Abi Saab, D., Mostarshedi, S., Basset, P., Protat, S., Angelescu, D., and Richalot, E. (2014) Effect of black silicon disordered structures distribution on its wideband reduced reflectance. *Mater. Res. Expr.*, **1**, 045045.

54 Abi Saab, D., Basset, P., Pierotti, M.J., Trawick, M.L., and Angelescu, D.E. (2014) Static and dynamic aspects of black silicon formation. *Phys. Rev. Lett.*, **113**, 265502.

55 Brückner, J.B., Le Rouzo, J., Escoubas, L., Berginc, G., Calvo-Perez, O., Vukadinovic, N., and Flory, F. (2013) Metamateriel filters at optical infrared frequencies. *Opt. Express*, **21** (14), 16992–17006.

56 Brückner, J.B., Brissonneau, V., Le Rouzo, J., Ferchichi, A., Gourgon, C., Dubarry, C., Berginc, G., and Escoubas, L. (2014) Inverted cones grating for flexible metafilter at optical and infrared frequencies. *Appl. Phys. Lett.*, **104**, 081114.

57 Gray, P.F. (1978) A method of forming diffusers of simple known statistical properties. *Optica Acta*, **25** (8), 765–775.

58 Mendez, E.R., Leskova, T.A., and Lopez, J.M. (2004) Design of two-dimensional random surfaces with specified scattering properties. *Opt. Lett.*, **29** (24), 2917–2919.

59 Garcia-Guerrero, E.E., Mendez, E.R., and Escamilla, H.M. (2007) Design and fabrication of random phase diffusers for extending the depth of focus. *Opt. Express*, **15**, 910–923.

60 Mendez, E.R., Garcia-Guerrero, E.E., Escamilla, H.M., Maradudin, A.A., Leskova, T.A., and Shchegrov, A.V. (2001) Photofabrication of random achromatic optical diffusers for uniform illumination. *Appl. Optics.*, **40**, 1098–1108.

61 Maradudin, A.A., Leskova, T.A., and Mendez, E.R. (2003) Two dimensional random surfaces that act as circular diffusers. *Opt. Lett.*, **28** (2), 72–74.

62 Elson, J.M. and Bennett, J.M. (1979) Relation between the angular dependence of scattering and the statistical properties of optical surfaces. *J. Opt. Soc. Am.*, **69** (1), 31–47.

63 Goldfischer, L. (1965) Autocorrelation function and power spectral density of laser-produced speckle patterns. *J. Opt. Soc. Am.*, **5** (3), 247–253.

64 Brissonneau, V., Flory, F., Escoubas, L., and Berginc, G. (2012) Statistically modified surfaces: experimental solutions for controlled scattered light. *J. Appl. Phys.*, **112**, 114325.

65 Ritchie, R.H. (1957) Plasma losses by fast electrons in thin films. *Phys. Rev.*, **106** (5), 874–881.

66 Kretschmann, E. and Reather, H. (1968) Radiative decay of nonradiative surface plasmon excited by light. *Z. Naturforsch*, **23A**, 2135–2136.

67 Otto, A. (1968) Excitation of nonradiative surface plasma waves in silver by the method of frustrated total reflection. *Z. Phys.*, **216** (4), 398–410.

68 Wang, A.X. and Kong, X. (2015) Review of recent progress of plasmonic materials and nano-structures for surface enhanced Raman scattering. *Materials*, **8**, 3024–3052.

69 Westphalen, M., Kreibig, U., Rostalski, J., Lüth, H., and Meissner, D. (2000) Metal cluster enhanced organic solar cells. *Sol. Energy Mater. Solar Cells*, **61**, 97–105.

70 Vedraine, S., Torchio, P., Duché, D., Flory, F., Simon, J.-J., Le-Rouzo, J., and Escoubas, L. (2011) Intrinsic absorption of plasmonic structures for organic solar cells. *Sol. Energy Mater. Solar Cells*, **95**, S57–S64.

71 Schmid, G. and Chi, L.F. (1998) Metal clusters and colloids. *Adv. Mater.*, **10.7**, 512–526.

72 Lin, H.J., Vedraine, S., Le Rouzo, J., Chen, S.H., Flory, F., and Lee, C.C. (2013) Optical properties of quantum dots layers: application to photovoltaic solar cells. *Sol. Energy Mater. Solar Cells*, **117**, 652–656.

73 Thierry, F. (2015) Etude des propriétés de nanoparticules semiconductrices pour les cellules solaires hybrids. PhD thesis, Aix-Marseille Université.

74 Andrae, D., Häußermann, U., Dolg, M., Stoll, H., and Preuß, H. (1990) Energy-adjusted *ab initio* pseudopotentials for the second and third row transition elements. *Theor. Chim. Acta*, **72** (2), 123–141.

75 Geerlings, P., De proft, F., and Langenaeker, W. (2003) Conceptual density functional theory. *Chem. Rev.*, **103** (5), 1793–1873.

76 Voon, L.C.L.Y. and Willatzen, M. (2009) *The kp Method: Electronic Properties of Semiconductors*, Springler-Verlag, Berlin.

77 Stoer, J. and Bulirsch, R. (2002) *Introduction to Numerical Analysis. Texts in Applied Mathematics*, Springer-Verlag, Berlin.

78 Jonsson, B., Eng, S.T. (1990) Solving the Schrödinger equation in arbitrary quantum-well potential profiles using the transfer matrix method. *IEEE J. Quantum Electron.*, **26** (11), 2025–2035.

79 Thierry, F., Le Rouzo, J., Flory, F., Berginc, G., and Escoubas, L. (2015) Fast and reliable approach to calculate energy levels in semiconductor nanostructures. *J. Nanophoton.*, **9** (1), 093080.

80 Inamdar, S.N., Ingole, P.P., Haram, S.K. (2008) Determination of band structure parameters and the quasi particle gap of CdSe quantum dots by cyclic voltammetry. *Chemphyschem.*, **9** (17), 2574–2579.

81 Ellingson, R.J., Beard, M.C., Johnson, J.C., Yu, P., Micic, O.I., Nozik, A.J., Shabaev, A., and Efros, A.L. (2005) Highly efficient multiple exciton generation in colloidal PbSe and PbS quantum dots. *Nano Lett.*, **5** (5), 865–871.

82 Choi, J.J., Wenger, W.N., Hoffman, R.S., Lim, Y.-F., Luria, J., Jasieniak, J., Marohn, J.A., and Hanrath, T. (2011) Solution-processed nano-crystal quantum dot tandem solar cells. *Adv. Mater.*, **23**, 3144–3148.

83 Chuang, C.H.M., Brown, P.R., Bulović, V., and Bawendi, Moungi G. (2014) Improved performance and stability in quantum dot solar cells through band alignment engineering. *Nat. Mater.*, **13**, 796–801.